Enhancement and destruction of spin-Peierls physics in a one-dimensional quantum magnet under pressure

Costel R. Rotundu,[1,*] Jiajia Wen,[1] Wei He,[1,2] Yongseong Choi,[3] Daniel Haskel,[3] and Young S. Lee[1,4]

[1]*Stanford Institute for Materials and Energy Sciences, SLAC National Accelerator Laboratory, 2575 Sand Hill Road, Menlo Park, California 94025, USA*

[2]*Department of Materials Science and Engineering, Stanford University, Stanford, California 94305, USA*

[3]*Advanced Photon Source, Argonne National Laboratory, Argonne, Illinois 60439, USA*

[4]*Department of Applied Physics, Stanford University, Stanford, California 94305, USA*

(Received 9 November 2017; revised manuscript received 1 February 2018; published 15 February 2018)

The application of pressure reveals a rich phase diagram for the quantum $S = 1/2$ spin chain material TiOCl. We performed x-ray diffraction on single-crystal samples in a diamond-anvil cell down to $T = 4$ K and pressures up to 14.5 GPa. Remarkably, the magnetic interaction scale increases dramatically with increasing pressure, as indicated by the high onset temperature of the spin-Peierls phase. The spin-Peierls phase was probed at ~6 GPa up to 215 K but possibly extends in temperature to above $T = 300$ K, indicating the possibility of a quantum singlet state at room temperature. Near the critical pressure for the transition to the more metallic phase, coexisting phases are exemplified by incommensurate order in two directions. Further comparisons are made with the phase diagrams of related spin-Peierls systems that display metallicity and superconductivity under pressure.

DOI: 10.1103/PhysRevB.97.054415

I. INTRODUCTION

Quantum magnets composed of interacting $S = 1/2$ magnetic ions exhibit a wide variety of phenomena with phases like quantum spin liquids and valence-bond crystals [1]. The application of pressure is a clean way to continuously adjust the interaction parameters to explore the ground-state physics. In one dimension, a fascinating ground state is the spin-Peierls state [2], arising from the coupling of $S = 1/2$ spins with the lattice in Heisenberg antiferromagnetic spin chain materials. A periodic deformation of the lattice (dimerization) along the chain takes place below a characteristic temperature T_{SP}. The deformation of the lattice enhances the exchange interaction between neighboring magnetic atoms that causes formation of singlet pairs of localized electrons (also known as a valence-bond crystal). This phase is robust, occurring in a minimal model involving nearest-neighbor magnetic exchange J and a coupling to three-dimensional phonons. The spin-Peierls transition has been observed in many organic compounds [3–5] but in only two inorganic systems, $CuGeO_3$ [6] and TiOCl [7,8]. However, $CuGeO_3$ is not an ideal realization of a spin-Peierls system due to the presence of significant next-nearest-neighbor exchange coupling along the chain [9]. TiOCl is an ideal realization which has been shown to undergo the canonical soft-phonon transition to the spin-Peierls state [8]. TiOCl crystalizes in an orthorhombic FeOCl-type structure in the space group $Pmmm$ with buckled Ti-O bilayers in the ab plane separated by Cl layers [Fig. 1(a)]. The Ti^{3+} ions, in the $3d^1$ electronic configuration, have an orbital arrangement forming quasi-one-dimensional $S = 1/2$ Heisenberg spin chains along the crystallographic b direction with a nearest-neighbor magnetic exchange of $J \approx 660$ K [7]. Adjacent chains are displaced by $b/2$, which leads to frustration of the interchain magnetic interaction, resulting in effectively decoupled spin chains. Here, we investigate the phase transitions of TiOCl as a function of pressure at low temperatures.

TiOCl exhibits two phase transitions at $T_{c2} \approx 92$ K and $T_{c1} \approx 66$ K at ambient pressure, corresponding to an incommensurately modulated state [8,10] and a commensurate state [8,11–13], respectively. At high temperatures, $T > T_{c2}$, the material is a paramagnetic Mott insulator, and at low temperatures, $T < T_{c1}$, the system is in a dimerized singlet state [Fig. 1(b)]. Below T_{c2}, the chains are dimerized with periodic discommensurations, and inelastic x-ray scattering of the soft phonon indicates that T_{c2} corresponds to the spin-Peierls transition temperature [8]. Below ≈150 K a pseudogap in the spin excitations has been reported [14–18]. Interestingly, similar gaps in the magnetic excitations of Mott insulators often appear in $S = 1/2$ quantum magnets, including the high-T_C cuprates. Calculations have suggested that TiOCl may be in the proximity of an insulator-to-metal transition, and further, it may become superconducting with doping [7,19–22] or application of pressure. The limited elemental doping performed to date on TiOCl showed no metallization. Two proposed paths not yet explored are doping of alkali metals together with organic ligands and the application of pressure on electron-doped TiOCl [22]. Application of high pressure on undoped TiOCl may be a promising route. An example of a spin-Peierls system exhibiting pressure-induced superconductivity is the organic compound $(TMTTF)_2PF_6$, where TMTTF = Tetramethyltetrathiafulvalene [23,24].

Optical measurements in the visible and infrared spectra suggest that the system becomes more metallic as the pressure

*rotundu@stanford.edu

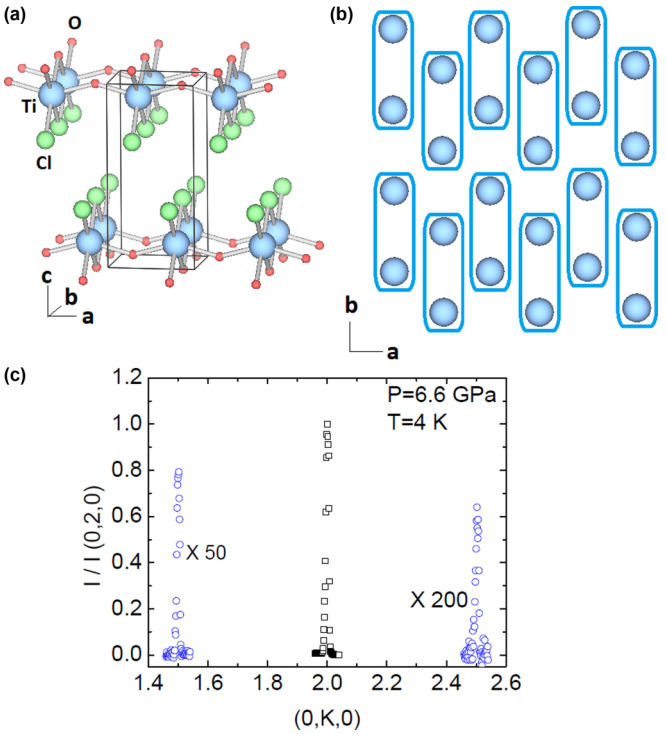

FIG. 1. Structure of TiOCl. (a) Crystal structure of TiOCl. (b) Representation of the commensurate dimer singlet state at $T < T_{c1}$ (the spin-Peierls state). (c) Scans along K through the commensurate (0,1.5,0) and (0,2.5,0) peak positions showing the peak intensity normalized to the nearest Bragg peak (0,2,0). For clarity, the superlattice peaks were magnified by a factor of 50 and 200, respectively.

is increased above ∼13 GPa [21,25–27]. Direct electrical resistivity measurements up to 24 GPa confirmed that the overall resistivity decreases about seven orders of magnitude [28] to a weaker insulator, but true metallization remains elusive. Early x-ray powder diffraction experiments revealed an orthorhombic $Pmmn$ to monoclinic $P2_1/m$ structural phase transition at 16 GPa in TiOCl [27] at room temperature. Later, it was found that aside from this structural transition at ≈15 GPa [21,29], there may be another structural transition at ≈22 GPa [21,29]. All the aforementioned structural experiments were performed on powders, where He gas was used as the pressure medium, with the exception of the experiments of Blanco-Canosa *et al.* [30], where a 4:1 CH_3OH:C_2H_5OH pressure medium was used and the low-pressure transition was found at ≈10 GPa. Prodi and coworkers studied the low-temperature ($T = 6$ K) single-crystal diffraction and found that the structural transition occurs at 13.1 GPa [31] when 4:1 methanol:ethanol was used as the pressure medium. The transition was accompanied by the destruction of the spin-Peierls dimerization and the appearance of an incommensurate charge-density wave perpendicular to the original spin-chain direction (b axis) [31]. This pressure-induced charge order is intriguing, which suggests that the more metallic state at high pressure has a Fermi surface which is gapped due to charge-density-wave order. As mentioned earlier, the weakening of the insulating behavior by over seven orders of magnitude gives hope that doping combined with the application of pressure may result in metallicity and perhaps even superconductivity.

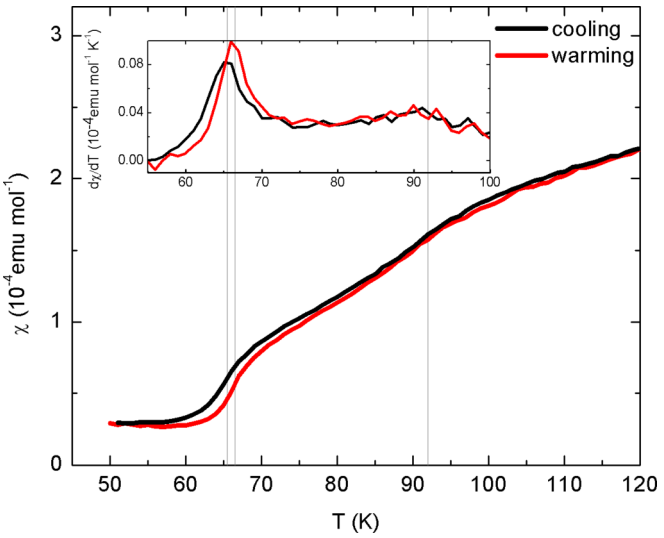

FIG. 2. Magnetic susceptibility as a function of temperature of a TiOCl single crystal in an applied magnetic field of $H = 1$ T parallel to the ab plane. The gray lines correspond to $T_{c2} = 92$ K when the system goes, upon cooling, to an incommensurate nearly dimerized state and to $T_{c1} = 66$ K when the system goes to a commensurate dimerized state. The first is a second-order transition, and the latter is a first-order transition based on the presence of the hysteresis.

Therefore, further investigation of the charge order and a full study of the temperature-pressure phase diagram has been performed to better understand this fascinating system. This was done with synchrotron x-ray diffraction on a single crystal in a high-pressure diamond-anvil cell down to $T = 4$ K and in pressures up to approximately 14.5 GPa.

II. EXPERIMENTAL METHODS

A. Materials and crystal growth

The single crystals of TiOCl were grown using the chemical-vapor transport method from $TiCl_3$ and TiO_2 in a closed quartz tube into a temperature gradient [7,32]. Thermal convection caused by the temperature gradient transports the material, with single crystals growing at the colder end of the tube. Typical dimensions of the grown crystals were a few square millimeters in the ab plane and 10–100 μm along the c axis (stacking direction). The purity of the crystals was checked by x-ray powder diffraction, and the orientation was confirmed using x-ray Laue method. The thickness of the as-grown crystal makes it ideal for the x-ray measurements without the need for cleaving or polishing. More in-depth characterization of the crystals was reported in earlier studies [8,31].

B. Bulk property measurements

Magnetization measurements were collected within a Quantum Design superconducting quantum interference device magnetic property measurement system magnetometer. Data showing magnetic susceptibility versus temperature are shown in Fig. 2. Because of the low signal the measurement was carried out in a moderately high magnetic field of 1 T (parallel to the crystallographic ab plane of the sample) on several coaligned crystals with a total mass of 2.5 mg. The very large

spin coupling constants make the two transitions insensitive to fields in this range.

C. High-pressure x-ray diamond-anvil cell

At 20 keV incident photon energy, the diamonds are nearly transparent, making them ideal for high-pressure x-ray scattering measurements. For the experiments, a Merrill-Bassett diamond-anvil cell (DAC) consisting of two opposing 800-μm culet diamonds was used. Type 301 stainless steel with an initial thickness of 250 μm was indented first between the two diamonds to about 140 μm thickness, and a centered 395-μm hole was drilled. Afterward, the gasket was placed on top of one of the anvils matching the indentation, the sample and a 30-μm^2 piece of 5-μm-thick silver foil were placed inside the drilled hole (sample chamber), and finally, the hole was filled with a 4:1 methanol:ethanol mixture that served as the pressure-transmitting medium. For the TiOCl sample, a crystal 40×60 μm^2 was cut from an $\approx$20-μm-thick larger crystal. When loaded, the ab plane of the sample was parallel to the diamond's culets. A ruby chip was placed in the chamber for loading pressure measurement. The expected change in thickness of the indented gasket filled with the 4:1 methanol:ethanol pressure medium at 50 GPa and 5 K is from 140-μm thickness down to 50 μm. The properties of the pressure-transmitting medium are discussed in the next section. Pressure was calibrated *in situ* against the lattice constant of silver, determined from position of three Bragg peaks [(200), (020), and (201)] of the silver foil inside the pressure chamber. A He-gas-driven membrane system was the generator of the applied force on the diamonds. The diamond-anvil cell was mounted on the cold finger of a closed-cycle cryostat with a base temperature of about 4 K.

D. Pressure-transmitting medium

The hydrostatic pressure medium closest to perfect up to high pressures is He gas. X-ray measurements at room temperature and 77 K up to 10 GPa showed also almost no difference in pressure gradients between He gas and the 4:1 methanol:ethanol mixture pressure medium [33]. Still, x-ray scattering measurements (which are the most relevant to our study) at 5 K and for pressures up to 20 GPa show equal levels of pressure inhomogeneity with $\Delta P/P$ per-unit area of $\pm 1.8\%/(10^4\ \mu\text{m}^2)$ [34]. While He gas is characterized by a constant deviatoric stress of 0.021 ± 0.011 GPa up to 16 GPa, 4:1 methanol:ethanol shows the same level of anisotropy up to 10 GPa, which slightly increases up to 16 GPa. Therefore, for low-temperature single-crystal x-ray diffraction, He and 4:1 methanol:ethanol are considered the best pressure media. The main disadvantage of He gas is its high compressibility, which causes the sample chamber to shrink significantly on gas loading under pressure. This reduces the sample-to-pressure-medium volume ratio. One other disadvantage of using He gas is, because of its diffusion, the generation of cracks and eventual failures in the diamonds [35] (at megabar pressures). But the choice of one over the other pressure medium in the present experiment was dictated by the pressure range of measurements and by the pressure-chamber-to-sample volume ratio [34], making the 4:1 methanol:ethanol mixture a better choice for the 10-GPa pressure range. For the TiOCl system, transmission measurements using the 4:1 methanol:ethanol mixture and argon gas (another close-to-hydrostatic pressure medium similar to He gas) showed results that qualitatively agree [25]. As a contrasting example, when CsI powder was used as the pressure medium, the pressure-induced structural effects occurred at lower pressure (with approximately 4 GPa) due to less hydrostatic conditions [25]. Blanco-Canosa *et al.* [30] used the less hydrostatic pressure medium CH_3OH:C_2H_5OH 4:1 for their x-ray scattering experiments and found a lower pressure for the $Pmmn$ to $P2_1/m$ structural transition, namely, $\approx$10 GPa.

E. X-ray diffraction measurements

Synchrotron x-ray diffraction experiments at high pressures and low temperatures were performed at the 4-ID-D beamline of the Advanced Photon Source at Argonne National Laboratory. The DAC was cooled in a ^{4}He closed-cycle cryostat that was installed on the sample stage of a Huber psi-circle diffractometer. The experiment was in transmission (Laue) geometry, where the x-ray beam traverses through the sample thickness and diffraction takes place in the vertical scattering plane. An incident x-ray energy of 20 keV was selected with a double-bounce Si(1 1 1) monochromator. A toroidal Pd mirror focused the beam to approximately $100 \times 200\ \mu\text{m}^2$ (vertical by horizontal). The beam size was further reduced with a slit to match the sample size. To maximize the **Q** resolution and eliminate uncertainties related to both the zero position and the overall scale of 2θ (which are issues commonly encountered with the image plate) a NaI point detector was used. The sample-detector distance was 1000 mm, and the detector slit size was 5 mm (horizontal) by 1 mm (vertical), giving a typical resolution of the instrument of less than $\Delta(\mathbf{Q}) \approx 4 \times 10^{-3}$ Å^{-1} [34]. All superlattice peaks were resolution limited at all pressures and temperatures along H and K. Throughout the text H, ΔH, K, ΔK, and L are in reciprocal lattice units (r.l.u.).

III. RESULTS

For the low-temperature single-crystal x-ray scattering measurements in a DAC, the pressure medium was selected to provide hydrostatic pressure yet remain solid in the parameter space of interest, so that the sample did not lose alignment. Here, we used a 4:1 methanol:ethanol mixture as the pressure medium. A helium-membrane-controlled diamond-anvil cell was used to allow the sample pressure to be changed *in situ* at the base temperature with better than 0.05 GPa resolution (see Sec. II). For mapping the complete T-P phase diagram for pressures up to 14.5 GPa and temperatures down to 4 K, we organized the experiment into three sets of measurements. The DAC was loaded and then compressed to about 0.3 GPa at room temperature, then cooled to 100 K, and finally compressed further to 6 GPa before cooling further to the base temperature of 4 K. The first set of measurements was carried out at a nominal pressure of 6 GPa at various temperatures on warming, within the range of $T = 4$–215 K. The second set of measurements was carried at a fixed temperature of 182 K while varying the pressure in the range 8–12 GPa. The purpose of these two sets of measurements is to determine

the high-temperature boundary of the phase diagram. A third set of measurements was performed at nominal pressures of 12 and 15 GPa for several temperatures in the 4–182 and 4–210 K ranges, respectively, with the aim of determining the high-pressure boundary of the phase diagram. The trajectories through the phase diagram were chosen to keep the pressure medium solid and hence maintain crystal alignment.

For the first set of measurements at the nominal pressure of 6 GPa, the differential thermal expansions of the gasket, diamonds, and the brass case of the cell cause the actual pressure inside the sample chamber to change slightly with temperature even if the pressure of the driving membrane mechanism is kept constant. The actual pressure at each temperature was measured, and typical values were 6.58 GPa at $T = 4$ K and 7.7 GPa at $T = 215$ K. Scans along the K direction through the commensurate (0,1.5,0) and (0,2.5,0) superlattice peak positions [normalized to the Bragg peak intensity at (0,2,0)] are shown in Fig. 1(c). For clarity, the superlattice peaks were magnified by 50 and 200, respectively. The temperature dependence of the dimerization is shown in Fig. 3(a), where K scans are plotted through the commensurate (0,1.5,0) peaks at 6 GPa for temperatures between 4 and 215 K. Above 182 K a new set of incommensurate peaks appear near positions (−0.08,1.5,0) and (0.08,1.5,0). It should be noted that the sudden drop in intensity (by a factor of 40) of the commensurate peak at 182 K coincides with the emergence of the incommensurate (±0.08,1.5,0) peaks. The K scans through the incommensurate (−0.08,1.5,0) peak position at the nominal pressure of 6 GPa for temperatures between 182 and 215 K are shown in Fig. 3(b). The $\Delta K = K - 1.5$ (r.l.u.) component of the displacement wave vector versus temperature for both (0,1.5,0) and (−0.08,1.5,0) peaks is shown in Fig. 3(c). The K position of the peaks was determined from Gaussian fits, and the error bars are less than or equal to the symbol size. The shaded area marks the temperature interval of coexistence of both commensurate (0,1.5,0) and incommensurate (−0.08,1.5,0) peaks (we will refer to this as the mixed phase). One other observation is that at 6 GPa the ΔK component of the displacement wave vector of the incommensurate peak is several orders smaller than that at ambient pressure [8].

The intensity of the incommensurate peak is about one order of magnitude smaller than that of the commensurate peak. Figure 4(a) shows H scans through the same superlattice peaks normalized to the nearby (0,2,0) Bragg peak at the nominal pressure of 6 GPa for temperatures between 4 and 215 K. At 182 K, incommensurate peaks appear near positions (−0.08,1.5,0) and (0.8,1.5,0). In the temperature interval 182–200 K the commensurate and incommensurate peaks coexist. The inset of Fig. 4(a) shows the area within the rectangle centered at $H = 0$ to more clearly depict the commensurate (0,1.5,0) peak intensities for temperatures from 182 to 215 K. At 215 K, the commensurate peak is entirely suppressed, leaving only the two incommensurate peaks. Figure 4(b) shows the normalized intensity of (H,1.5,0) peaks vs temperature. The intensity of the commensurate (0,1.5,0) peak drops rapidly when the system enters the mixed phase, consistent with the same observation from the K scans [Fig. 3(a)]. This is also consistent with the observed rapid drop in intensity at T_{c1} in ambient-pressure conditions [8]).

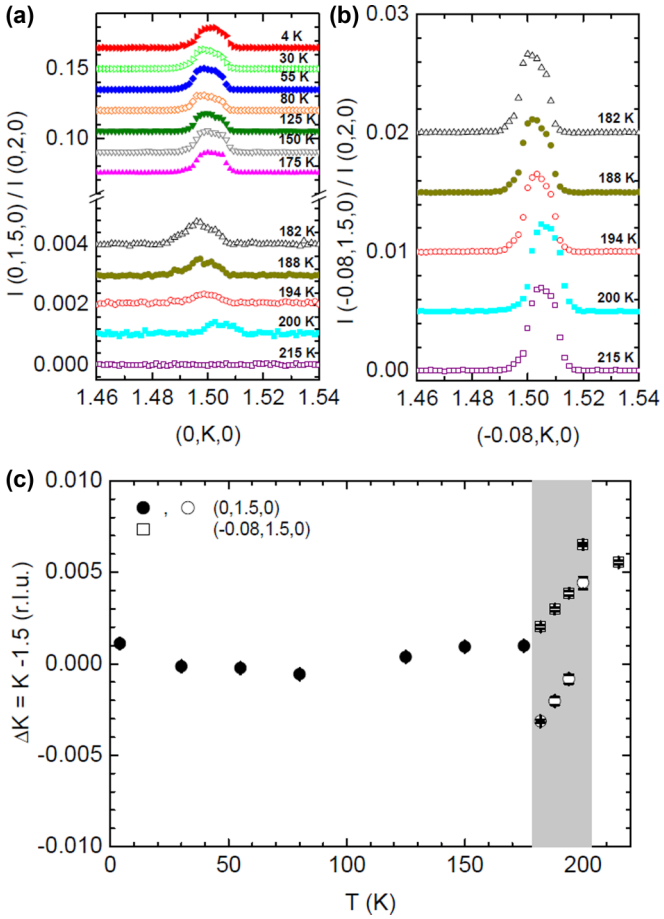

FIG. 3. Temperature dependence of the superlattice reflections (H,1.5,0) at the nominal pressure 6 GPa: Scans along K. (a) Scans along K through the (0,1.5,0) peak position at the nominal pressure 6 GPa for temperatures between 4 and 215 K. (b) Scans along K through the (−0.08,1.5,0) peak position for temperatures between 182 and 215 K. (c) $\Delta K = K - 1.5$ (r.l.u.) vs T for both (0,1.5,0) and (−0.08,1.5,0) peaks. The shaded area marks the temperature interval of coexistence of both commensurate (0,1.5,0) and incommensurate (−0.08,1.5,0) peaks. The error bars are smaller than the size of the symbols.

The incommensurate modulation along the a direction continues to evolve as a function of pressure. Figure 5(a) shows H scans at $T = 182$ K for several pressures in the 8–12-GPa range. This set of scans provides information on the high-temperature boundary of the T-P phase diagram. Within this pressure range, the H scans show both commensurate (0,1.5,0) and incommensurate (≈ ±0.08,1.5,0) peaks up to 11.5 GPa. At 12 GPa the commensurate peak is suppressed, leaving only the incommensurate peaks. Figure 5(b) plots $\Delta H = (H_+ - H_-)/2$ versus pressure at 182 K. H_+ and H_- are determined from fits of the peaks with Gaussians. The error bars in Fig. 5(b) are smaller than or equal to the size of the symbols. With the application of pressure, the incommensurability rapidly increases. At this temperature (182 K), pressure has a rather strong effect on the incommensurability of the (≈ ±0.08,1.5,0) superlattice peak.

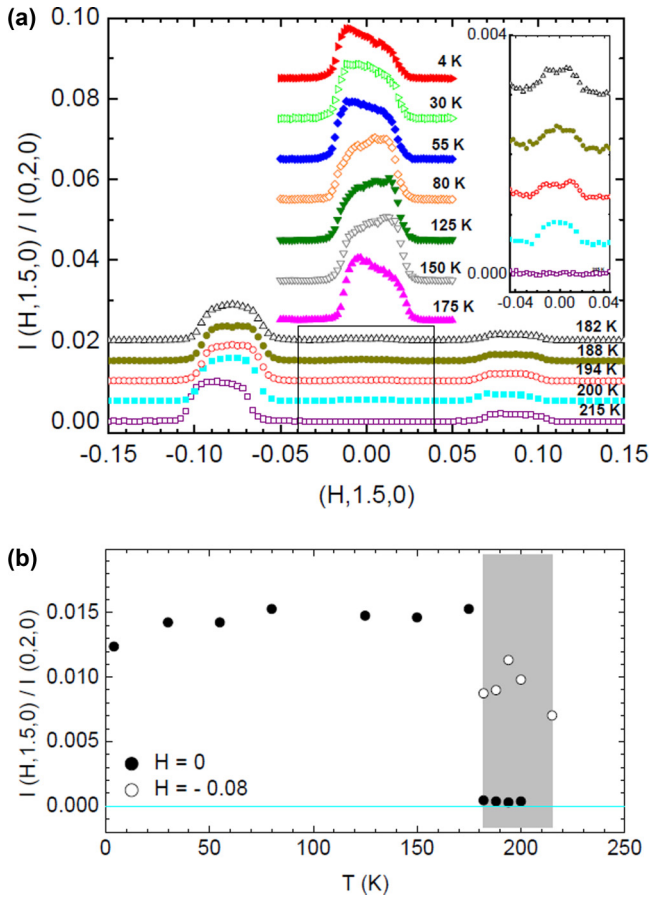

FIG. 4. Temperature dependence of the superlattice reflections $(H,1.5,0)$ at the nominal pressure 6 GPa: H scans. (a) Scans along the $(H,1.5,0)$ direction at the nominal pressure 6 GPa for temperatures between 4 and 215 K. Below 175 K there is only the commensurate peak at $H = 0$. Between 200 and 182 K both the commensurate (0,1.5,0) and incommensurate $(\pm 0.08,1.5,0)$ peaks are present. At 215 K only the incommensurate $(\pm 0.08,1.5,0)$ peaks are present. The inset is a magnification of the data in the black rectangle centered at $H = 0$. (b) Integrated intensity of the superlattice peaks as a function of temperature.

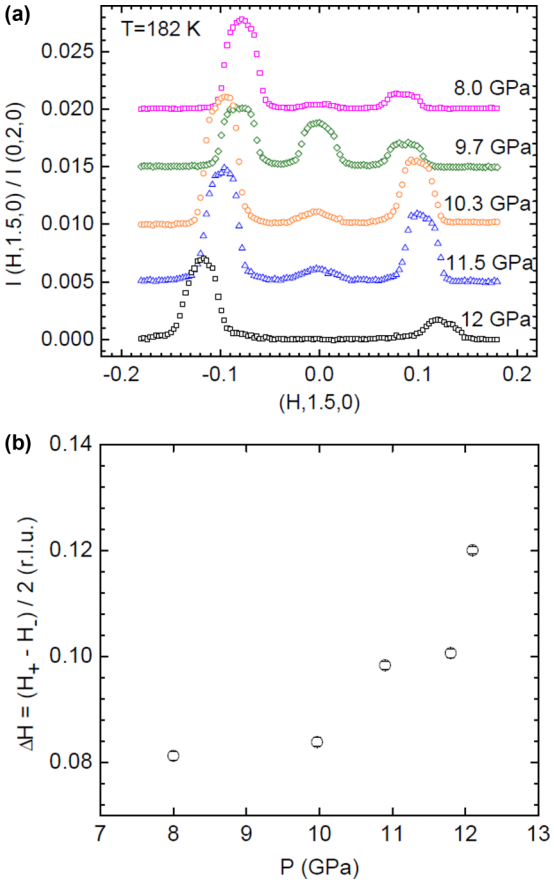

FIG. 5. Pressure dependence of the superlattice reflections $(H,1.5,0)$ at 182 K. (a) $(H,1.5,0)$ scans at 182 K for different pressures. (b) The incommensurate wave vector (relative to the commensurate dimerized superlattice position) as a function of pressure at $T = 182$ K.

Previous x-ray studies by Prodi *et al.* [31] revealed the emergence of a new ground state for pressures above ~13 GPa, characterized by a pair of incommensurate superlattice peaks with a modulation vector $\delta_a = 0.48$ along the a axis (which is perpendicular to the low-pressure spin chain direction). These peaks arise above the critical pressure of the more metallic state and may be related to charge-density-wave ordering in a more two-dimensional electronic system. We observed similar a-axis modulations and found that this new phase exists over an extended pressure and temperature range. Figure 6 shows the incommensurate a-axis modulation reflections at (1.52,0,0) and (2.48,0,0). Figure 6(a) shows longitudinal scans through the peaks normalized to the nearby (2,0,0) Bragg peak intensity at $P = 12.8$ GPa and $T = 100$ K. Figure 6(b) shows longitudinal scans as a function of pressure at 100 K for $P = 12.8$ and 14.4 GPa. As expected, the a-axis modulation disappears at 6 GPa and $T = 100$ K, which is well below the critical pressure.

IV. DISCUSSION

Our observations of weak x-ray superlattice peaks in high pressures shed light on two important aspects of the spin-Peierls physics in TiOCl. First, the application of pressure dramatically enhances the magnetic energy scale and hence the critical phase boundary for the dimerization transition. Second, near the critical pressure of ~ 13 GPa, the commensurate superlattice peaks disappear; however, incommensurate modulations of the structure remain. In fact, the modulations are characterized by two types of discommensurations: around both the $(0,2 \pm 0.5,0)$ and $(2 \pm 0.5,0,0)$ peaks (using the low-temperature orthorhombic notation). Our main results can be summarized in the phase diagram depicted in Fig. 7. It had been hypothesized from high-pressure magnetization measurements that, if the increase rate of the transitions remains constant $(\partial \ln T_{c1}/\partial P) = 2.88 \times 10^{-1}$ 1/GPa and $(\partial \ln T_{c2}/\partial P) = 3.4 \times 10^{-1}$ 1/GPa, the spin-Peierls transition should reach room temperature at a pressure somewhere around 6 GPa [30]. Our high-temperature x-ray scattering data provide unique evidence of the dimerization transition temperature in high pressures. We find that T_{c1} appears to increase almost linearly with pressure up to at least 7 GPa. Therefore, TiOCl under pressure (>7 GPa) is likely a unique example of a room-temperature

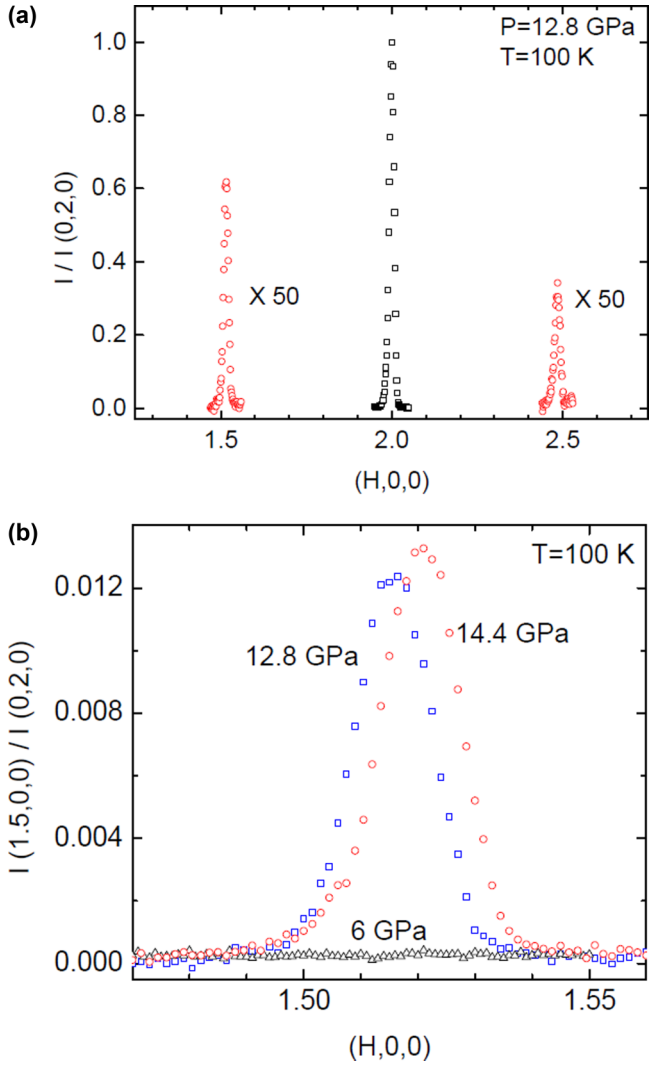

FIG. 6. The high-pressure incommensurate a-axis modulation reflections near (1.5,0,0) and (2.5,0,0). (a) Scans along K through the (1.5,0,0) and (2.5,0,0) peak positions showing the intensity normalized to the nearby (2,0,0) Bragg peak at $P = 12.8$ GPa and $T = 100$ K. (b) H scans through the (1.5,0,0) peak at 100 K for $P = 12.8$ and 14.4 GPa. At 6 GPa, there is no discernible a-axis modulation peak.

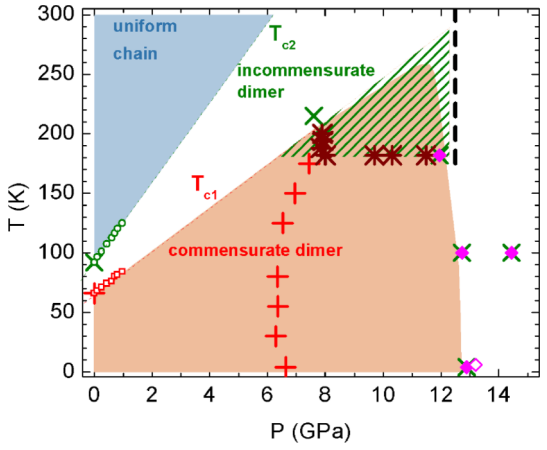

FIG. 7. T-P phase diagram of TiOCl. Pluses mark the commensurate peaks (commensurate dimer phase), crosses mark the incommensurate peaks (incommensurate dimer phase), asterisks mark the "mixed" phase (coexistence of both commensurate and incommensurate phases), solid diamonds marks the incommensurate a-axis modulation peak, the open diamond marks the original a-axis modulation peak from Prodi *et al.* [31], and the squares and circles mark the transitions T_{c1} and T_{c2} from the corresponding peaks in $d\chi(T)/dT$, adapted from Blanco-Canosa *et al.* [30]. The vertical dashed line marks the resistivity crossover [21,28], in the vicinity of the orthorhombic $Pmmn$ to monoclinic $P2_1/m$ structural phase transition (see text).

quantum singlet state. This is facilitated by the large exchange constant $J \approx 660$ K [7,36] at ambient pressure, the highest reported among spin-Peierls compounds. It has been estimated from $(\partial \ln T/\partial P) = 4.6 \times 10^{-1}$ 1/GPa and $T_{SP} \propto J$ that at a pressure of 9 GPa the direct exchange interaction J is 3300 K [30], which would be the highest known exchange coupling in a quantum magnet (for instance, in La_2CuO_4, $J \approx 1500$ K, and in Sr_2CuO_3, $J \approx 2800$ K [37] in ambient pressure).

We can compare the phase diagrams of TiOCl with the phase diagram of another spin-Peierls system, the organic $(TMTTF)_2PF_6$, which becomes superconducting at 4 GPa (up to 7 GPa) [23,24]. The phase diagram of $(TMTTF)_2PF_6$ is, in fact, more general, being common to Fabre and Bechgaard salts [24,38,39] and to the organic superconductors [40]. With the application of pressure, in both $(TMTTF)_2PF_6$ and TiOCl, density-wave order emerges at higher pressures beyond the spin-Peierls state. The pressure-induced metallic phase present in $(TMTTF)_2PF_6$ was not yet reached in TiOCl, but within the highest pressure measured to date (24 GPa), a large 10^7-fold decrease in the overall electrical resistivity has been reported, as mentioned earlier [28]. The fastest decrease in overall resistivity with application of pressure takes place for pressures up to 13 GPa, critical pressure coinciding with fastest decrease of the activation energy [28]. This pressure of the resistivity crossover (between insulator and weak insulator) is marked in Fig. 7 by the vertical dashed line. Therefore, the similarity in the phase diagram of the two spin-Peierls systems is another hint of possible metallization at very high pressures. The relatively higher critical pressures of the different ground states in TiOCl compared with those in $(TMTTF)_2PF_6$ may be related to the overall larger energy scale J of TiOCl compared to the other spin-Peierls systems. The pressure medium (steatite) used in the $(TMTTF)_2PF_6$ experiments [24] (as discussed in Sec. II) is less hydrostatic, and it may be that uniaxial forces play a vital role in the transitions. It is known, for instance, that the temperature-strain phase diagram of the organic α-$(BEDT\text{-}TTF)_2I_3$, where BEDT-TTF stands for bisethylenedithio-tetrathiafulvalen displays superconductivity only with the strain along the a axis [41]. Similar strain studies on TiOCl should also be pursued.

In this paper, using synchrotron x-ray scattering on a TiOCl single crystal in a diamond-anvil cell, we determined the phase diagram for this spin-Peierls system down to $T = 4$ K and in pressures up to 14.5 GPa. Scans through the commensurate $(0,1.5,0)$ position at a pressure of $\sim$7 GPa revealed incommensurate peaks persisting to the highest measured temperatures.

These measurements reveal a region of coexistence in the phase diagram. At higher pressures (above around 12 GPa) the commensurate peak is suppressed, leaving only the incommensurate modulation. Further, the incommensurate a-axis modulation peaks at (1.52,0,0) and (2.48,0,0) reveal a charge-density-wave phase that exists over an extended region of the phase diagram. This region of the phase diagram corresponds to the more metallic phase of TiOCl. The dramatic increase of the spin-Peierls temperature with pressure indicates that TiOCl appears to be an example of a quantum singlet ground state at room temperature. To further test the applicability of the soft-phonon mechanism of the transition, future measurements of the phonons and spin excitations in comparable pressures would be most instructive.

ACKNOWLEDGMENTS

The work at SLAC was supported by the U.S. Department of Energy (DOE), Office of Science, Basic Energy Sciences, Materials Sciences and Engineering Division, under Contract No. DE-AC02-76SF00515 (sample preparation, x-ray scattering, and data analysis). Work at Argonne is supported by the U.S. Department of Energy, Office of Science, Office of Basic Energy Sciences under Contract No. DE-AC-02-06CH11357.

[1] P. W. Anderson, Mater. Res. Bull. **8**, 153 (1973).
[2] E. Pytte, Phys. Rev. B **10**, 4637 (1974).
[3] J. W. Bray, H. R. Hart, Jr., L. V. Interrante, I. S. Jacobs, J. S. Kasper, G. D. Watkins, S. H. Wee, and J. C. Bonner, Phys. Rev. Lett. **35**, 744 (1975).
[4] I. S. Jacobs, J. W. Bray, H. R. Hart, Jr., L. V. Interrante, J. S. Kasper, G. D. Watkins, D. E. Prober, and J. C. Bonner, Phys. Rev. B **14**, 3036 (1976).
[5] S. Huizinga, J. Kommandeur, G. A. Sawatzky, B. T. Thole, K. Kopinga, W. J. M. de Jonge, and J. Roos, Phys. Rev. B **19**, 4723 (1979).
[6] M. Hase, I. Terasaki, and K. Uchinokura, Phys. Rev. Lett. **70**, 3651 (1993).
[7] A. Seidel, C. A. Marianetti, F. C. Chou, G. Ceder, and P. A. Lee, Phys. Rev. B **67**, 020405(R) (2003).
[8] E. T. Abel, K. Matan, F. C. Chou, E. D. Isaacs, D. E. Moncton, H. Sinn, A. Alatas, and Y. S. Lee, Phys. Rev. B **76**, 214304 (2007).
[9] J. Riera and A. Dobry, Phys. Rev. B **51**, 16098 (1995).
[10] M. Shaz, S. van Smaalen, L. Palatinus, M. Hoinkis, M. Klemm, S. Horn, and R. Claessen, Phys. Rev. B **71**, 100405(R) (2005).
[11] R. Ruckamp, J. Baier, M. Kriener, M. W. Haverkort, T. Lorenz, G. S. Uhrig, L. Jongen, A. Möller, G. Meyer, and M. Grüninger, Phys. Rev. Lett. **95**, 097203 (2005).
[12] A. K. J. Strempfer, B. Bohnenbuck, B. Keimer, M. Hoinkis, M. Klemm, S. Horn, A. Loidl, M. Sing, R. Claessen, and M. v. Zimmermann, Phys. Rev. B **73**, 172413 (2006).
[13] A. Schönleber, S. van Smaalen, and L. Palatinus, Phys. Rev. B **73**, 214410 (2006).
[14] T. Imai and F. C. Chou, arXiv:cond-mat/0301425.
[15] G. Caimi, L. Degiorgi, N. N. Kovaleva, P. Lemmens, and F. C. Chou, Phys. Rev. B **69**, 125108 (2004).
[16] P. Lemmens, K. Y. Choi, G. Caimi, L. Degiorgi, N. N. Kovaleva, A. Seidel, and F. C. Chou, Phys. Rev. B **70**, 134429 (2004).
[17] J. Hemberger, M. Hoinkis, M. Klemm, M. Sing, R. Claessen, S. Horn, and A. Loidl, Phys. Rev. B **72**, 012420 (2005).
[18] J. P. Clancy, B. D. Gaulin, K. C. Rule, J. P. Castellan, and F. C. Chou, Phys. Rev. B **75**, 100401(R) (2007).
[19] R. J. Beynon and J. A. Wilson, J. Phys. Condens. Matter **5**, 1983 (1993).
[20] L. Craco, M. S. Laad, and E. Müller-Hartmann, J. Phys. Condens. Matter **18**, 10943 (2006).
[21] C. A. Kuntscher, M. Klemm, S. Horn, M. Sing, and R. Claessen, Eur. Phys. J. Spec. Top. **180**, 29 (2010).
[22] Y. Z. Zhang, K. Foyevtsova, H. O. Jeschke, M. U. Schmidt, and R. Valentí, Phys. Rev. Lett. **104**, 146402 (2010).
[23] T. Adachi, E. Ojima, K. Kato, H. Kobayashi, T. Miyazaki, M. Tokumoto, and A. Kobayashi, J. Am. Chem. Soc. **122**, 3238 (2000).
[24] D. Jaccard, H. Wilhelm, D. Jérome, J. Moser, C. Carcel, and J. M. Fabre, J. Phys. Condens. Matter **13**, L89 (2001).
[25] C. A. Kuntscher, S. Frank, A. Pashkin, M. Hoinkis, M. Klemm, M. Sing, S. Horn, and R. Claessen, Phys. Rev. B **74**, 184402 (2006).
[26] C. A. Kuntscher, S. Frank, A. Pashkin, H. Hoffmann, A. Schönleber, S. van Smaalen, M. Hanfland, S. Glawion, M. Klemm, M. Sing, S. Horn, and R. Claessen, Phys. Rev. B **76**, 241101(R) (2007).
[27] C. A. Kuntscher, A. Pashkin, H. Hoffmann, S. Frank, M. Klemm, S. Horn, A. Schönleber, S. van Smaalen, M. Hanfland, S. Glawion, M. Sing, and R. Claessen, Phys. Rev. B **78**, 035106 (2008).
[28] M. K. Forthaus, T. Taetz, A. Möller, and M. M. Abd-Elmeguid, Phys. Rev. B **77**, 165121 (2008).
[29] J. Ebad-Allah, A. Schönleber, S. van Smaalen, M. Hanfland, M. Klemm, S. Horn, S. Glawion, M. Sing, R. Claessen, and C. A. Kuntscher, Phys. Rev. B **82**, 134117 (2010).
[30] S. Blanco-Canosa, F. Rivadulla, A. Piñeiro, V. Pardo, D. Baldomir, D. I. Khomskii, M. M. Abd-Elmeguid, M. A. López-Quintela, and J. Rivas, Phys. Rev. Lett. **102**, 056406 (2009).
[31] A. Prodi, J. S. Helton, Y. Feng, and Y. S. Lee, Phys. Rev. B **81**, 201103(R) (2010).
[32] H. Schäfer, F. Wartenpfuhl, and E. Weise, Z. Anorg. Allg. Chem. **295**, 268 (1958).
[33] N. Tateiwa and Y. Haga, Rev. Sci. Instrum. **80**, 123901 (2009).
[34] Y. Feng, R. Jaramillo, J. Wang, Y. Ren, and T. F. Rosenbaum, Rev. Sci. Instrum. **81**, 041301 (2010).
[35] A. Dewaele and P. Loubeyre, J. Appl. Phys. **99**, 104906 (2006).
[36] V. Kataev, J. Baier, A. Moller, L. Jongen, G. Meyer, and A. Freimuth, Phys. Rev. B **68**, 140405(R) (2003).
[37] A. C. Walter, T. G. Perring, J.-S. Caux, A. T. Savici, G. D. Gu, C.-C. Lee, W. Ku, and I. A. Zaliznyak, Nat. Phys. **5**, 867 (2009).
[38] W. Yu, F. Zhang, F. Zamborszky, B. Alavi, A. Baur, C. A. Merlic, and S. E. Brown, Phys. Rev. B **70**, 121101(R) (2004).
[39] M. Dressel, Naturwissenschaften **94**, 527 (2007).
[40] D. Jérome, Science **252**, 1509 (1991).
[41] N. Tajima, J.-I. Fujisawa, N. Naka, T. Ishihara, R. Kato, and Y. Nishio, J. Phys. Soc. Jpn. **71**, 1832 (2002).